Modelling of the low-impulse blast behaviour of fibre-metal laminates based on different aluminium alloys

Thuc P. Vo*, Z.W. Guan, W.J. Cantwell and G.K. Schleyer

School of Engineering, University of Liverpool, Brownlow Street, Liverpool L69 3GQ, UK.

Abstract

A parametric study has been undertaken in order to investigate the influence of the properties of the aluminium alloy on the blast response of fibre-metal laminates (FMLs). The finite element (FE) models have been developed and validated using experimental data from tests on FMLs based on a 2024-O aluminium alloy and a woven glass-fibre/polypropylene composite (GFPP). A vectorized user material subroutine (VUMAT) was employed to define Hashin's 3D rate-dependant damage constitutive model of the GFPP. Using the validated models, a parametric study has been carried out to investigate the blast resistance of FML panels based on the four aluminium alloys, namely 2024-O, 2024-T3, 6061-T6 and 7075-T6. It has been shown that there is an approximation linear relationship between the dimensionless back face displacement and the dimensionless impulse for all aluminium alloys investigated here. It has also shown that the residual displacement of back surface of the FML panels and the internal debonding are dependent on the yield strength of the aluminium alloy.

Keywords: A. Glass fibres; B. Mechanical properties; C. Damage mechanics; C. Numerical analysis.

* Corresponding author, Tel.: +44 151 7945095; Fax: +44 151 7945218.

Present address: School of Mechanical, Aeronautical and Electrical Engineering, Glyndwr University, Mold Road, Wrexham LL11 2AW, UK.

E-mail address: t.vo@glyndwr.ac.uk

1. Introduction

Fibre-metal laminates (FMLs) are hybridised metal and composite structural materials that have been attracting interest from a number of researchers due to their improved fatigue and impact resistance ([1]-[6]). The most commonly used FML is GLARE, which comprises thin aluminium 2024-T3 sheets and a unidirectional or a biaxial glass-fibre-reinforced epoxy. The blast response of FMLs has received attention in a number of experimental studies. Fleischer [7] presented data from blast test results on a lightweight luggage container based on GLARE and reported that it was capable of withstanding a bomb blast greater than that in the Lockerbie air disaster. Langdon et al. ([8]-[10]) carried out blast tests of FML panels based on a 2024-O aluminium alloy and a glass fibre reinforced polypropylene. They observed a number of failure mechanisms including multiple debonding, large plastic displacements, fibre fracture and matrix cracking. Diamond, cross-shaped back face damage and front face buckling were also observed. A dimensionless analysis showed that the front and back face displacements fell within one plate thickness of a linear trend line. Blast tests on FML panels based on other composites, such as a glass fibre polyamide matrix and GLARE were also been undetaken by Langdon et al. ([11], [12]). Since experimental trials are usually very costly and time-consuming, it is evident that modelling the blast behaviour of FMLs using commercial finite element software would be great interest. Once these models are verified, they can be used to predict the response of FMLs based on different configurations, lay-ups, loading and boundary conditions without the need to undertake a large number of experimental tests. However, in spite of the fact that there have been a number of experimental studies on the blast behaviour of FMLs, relatively little work has been conducted to model their response. Kotzakolios et al. [13] used LS-DYNA to investigate the blast response of GLARE laminates-comparison against experimental results. This work also included the numerical verification process for 50, 75, 100, 150 gram of explosive, and

discusses the corresponding failure modes and strain rates. Later, Kotzakolios et al. [14] extended their research to investigate the damage induced in a typical commercial fuselage based on aluminium and GLARE, when subjected to an explosive charge. Simulations were performed for different charge locations in three stages: an initialization phase, a blast phase and a final phase. Soutis et al. [15] investigated the structural response of fully clamped GLARE panels to blast loads using LS-DYNA. Excellent agreement between the predicted and measured midpoint deflections and evidence of significant yield line deformation were highlighted. Karagiozova et al. [16] modelled the blast response of FML panels based on various stacking configurations using ABAQUS/Explicit in order to predict the influence of the loading parameters and structural characteristics on their overall behaviour. Although ABAQUS has a number of failure criteria for composite materials, they can only used with 2D elements, such as plane stress and continuum shell elements. Further, none of these criteria consider strain-rate effects in composite materials, which is clearly important in dynamic studies. The 2D elements, with the existing failure criteria, are not capable of taking large through-the-thickness rate-dependent deformations into account. Therefore, it is necessary to develop a constitutive model with associated failure criteria suitable for simulating a composite material using 3D solid elements. Recently, Vo et al. [17] developed FE models which were validated using experimental data from tests on FMLs based on a 2024-O aluminium alloy and a woven glass-fibre/polypropylene composite. The rate-dependent failure criteria for a unidirectional composite were used, which were based on the modified Hashin's 3D failure criteria [18]. The constitutive model and failure criteria were then implemented in ABAQUS/Explicit using the VUMAT subroutine. Here, the analysis was restricted to low-impulse blast behaviour, which was defined according to Mode I failure from the experimental study carried out by Langdon et al. ([8]-[10]).

In this paper, based on the previous research [17], parametric studies were carried out to

investigate the influence of the properties of the aluminium alloy on the blast resistance of FMLs for aerospace applications. Here Johnson-Cook strain hardening and damage criterion were employed. Particular attention is given to predicting the front and back displacements and the energies dissipated during the blast process. In total, thirty-six cases are studied. It has been shown that there is an approximation linear relationship between the dimensionless back face displacement and the dimensionless impulse for all aluminium alloys investigated here. It has also shown that the residual displacement of back surface of the FML panels and the internal debonding are dependent on the yield strength of the aluminium alloy.

2. Geometric and Blast Loadings of FML Panels

For verification purposes, the FML panels previously subjected to localised blast loading in the experimental study by Langdon et al. ([8]-[10]) are used to validate the curent FE models. These 400×400 mm panels (300×300 mm exposed area), were manufactured from sheets of 0.025 in. (approximately 0.6 mm) thick 2024-O aluminium alloy and a woven glass-fibre/polypropylene composite. The FML panels are identified using the notation, AXTYZ-#, as described in [8], where A = aluminium, X = number of aluminium layers, T = GFPP, Y = number of blocks of GFPP, Z = number of plies of GFPP per block and # indicates the panel number. In order to promote better adhesion to the composite material, a thin layer of polypropylene (PP) film (Xiro 23.101) was placed between the chromate-coated aluminium alloy and the glass fibre reinforced PP composite. The panels were tested using a ballistic pendulum facility.

In order to investigate the influence of the properties of the aluminium alloy on the low-impulse blast behavior, FML panels based on the four aluminium alloys, namely 2024-O, 2024-T3, 6061-T6 and 7075-T6, subjected to an impulse I = 8 Ns were considered. All four alloys are widely used in the aerospace industry. Details of the lay-ups and impulses investigated in this study are listed in Table 1.

The current research is concentrated on the cases where the explosive is placed on the surface of the target. Therefore, converting the explosion to a surface impulsive pressure is likely to be the most effective approach [16, 19, 20]. However, if the explosive is detonated at some distance from the target, Arbitrary Lagrangian Eulerian (ALE) and CONWEP [21] should be used to apply the blast load to the structure. Ideally, during an air-blast event, air and detonation products, as well as the structural response of the target should be considered simultaneously. Using the ALE approach, air and the detonation products may be described using an Eulerian formulation in a gaseous domain, while the structural response can be treated in a structural domain. A coupling algorithm for the fluid–structure interaction is then employed to connect the two domains [14, 15]. However, this approach requires considerably more computational time, especially for ABAQUS/Explicit. A blast analysis using the pressure time history predicted by CONWEP or similar is likely save computational time and is likely to produce a reasonably accurate response. For the reasons mentioned the above, the blast load in this study is assumed to act impulsively and is applied using a pressure load acting on the exposed face of the FML panel [16]. This pressure load, calculated from the measured impulse, is a function of both time and distance from the plate centre. The pressure–time history is idealized as a uniform function over a small central region and follows an exponentially decaying function as:

$$P(r,t) = p_1(r)\,p_2(t) \tag{1}$$

where:

$$\begin{aligned} p_1(r) &= \begin{cases} P_0 & r \le r_0 \\ P_0 e^{-k(r-r_0)} & r_0 < r < r_b \\ 0 & r > r_b \end{cases} \\ p_2(t) &= e^{-2t/t_0} \end{aligned} \tag{2}$$

where r_0 = 15 mm is the radius of the explosive disc used in the experiments, $r_b < L/2$, L is the length of the panel and t_0 = 0.008 ms is the characteristic decay time for the pulse and k is

an exponential decay parameter. The decay parameter is not constant, but a function of the total impulse [16]. The total impulse is defined as:

$$I = 2\pi \int_0^{\infty} \int_0^{r_b} P(r,t) dr dt \tag{3}$$

A user subroutine VDLOAD was used to model the pressure distribution over the exposed area of the plate.

3. Material Modelling

3.1 Aluminium layers

The aluminium alloy was modeled as an elasto-plastic material, exhibiting rate-dependent behaviour. Temperature effects in the aluminium alloy were not taken into account. The Johnson-Cook material model was used in the form:

$$\sigma = \left[A + B(\bar{\varepsilon}_{pl})^n \right] \left[1 + C \ln \left(\frac{\dot{\bar{\varepsilon}}_{pl}}{\dot{\varepsilon}_0} \right) \right] \tag{4}$$

where $\bar{\varepsilon}_{pl}$ is the equivalent plastic strain; $\dot{\bar{\varepsilon}}_{pl}$ and $\dot{\varepsilon}_0$ are the equivalent plastic and reference strain rate and *A*, *B*, C and *n* are material parameters.

Damage in the Johnson-Cook material model is predicted using the following cumulative damage law:

$$D = \sum \left(\frac{\Delta \bar{\varepsilon}_{pl}}{\bar{\varepsilon}_f^{pl}} \right) \tag{5}$$

in which:

$$\bar{\varepsilon}_f^{pl} = \left[D_1 + D_2 \exp\left(D_3 \sigma^* \right) \right] \left[1 + D_4 \ln \left(\frac{\dot{\bar{\varepsilon}}_{pl}}{\dot{\varepsilon}_0} \right) \right] \tag{6}$$

where $\Delta \bar{\varepsilon}_{pl}$ is the increment of equivalent plastic strain during an increment in loading and

σ^* is the mean stress normalised by the equivalent stress. The parameters D_1, D_2, D_3, and D_4 are constants. Failure is assumed to occur when D = 1. Hence the current failure strain, $\bar{\varepsilon}_f^{pl}$, and thus the accumulation of damage, D, is a function of the mean stress and the strain rate. The constants in the Johnson-Cook model for the four alluminium alloys used in this study are given in Table 2. The Young's modulus, Poisson's ratio and density of the various aluminium alloys were taken as E = 73.1 GPa, ν = 0.3 and ρ = 2690 kg/m^3, respectively.

3.2 Glass fibre reinforced composite layers

3.2.1 The 3D damage model for the composite material

Given that a woven glass-fibre/polypropylene composite layer is produced by placing fibres in a [0^0/90^0] pattern, the material behaviour within the plane of the laminate is similar in those two directions. There is therefore no need to separate the fibre and resin in order to simulate the overall response of the composite ply. Besides, the material tests carried out in this paper were based on the composite laminates, i.e. no individual tests to address fiber and resin separately. Therefore, Hashin's 3D failure criteria [18] are sufficient to simulate woven glass-fibre/polypropylene composite layer. The failure functions may be expressed as follows:

$$\text{Fibre tension } (\sigma_{11} \geq 0)\text{: } F_{\mathrm{f}}^{\mathrm{t}} = \left(\frac{\sigma_{11}}{X_{1t}}\right)^2 + \left(\frac{\sigma_{12}}{S_{12}}\right)^2 + \left(\frac{\sigma_{13}}{S_{13}}\right)^2,\ d_{ft} = 1$$

$$\text{Fibre compression } (\sigma_{11} < 0)\text{: } F_{\mathrm{f}}^{\mathrm{c}} = \frac{|\sigma_{11}|}{X_{1c}},\ d_{fc} = 1$$

$$\text{Matrix tension } (\sigma_{22} + \sigma_{33} \geq 0)\text{: } F_{\mathrm{m}}^{\mathrm{t}} = \frac{(\sigma_{22} + \sigma_{33})^2}{X_{2t}^2} + \frac{\sigma_{23}^2 - \sigma_{22}\sigma_{33}}{S_{23}^2} + \frac{\sigma_{12}^2 + \sigma_{13}^2}{S_{12}^2},\ d_{mt} = 1$$

$$\text{Matrix compression } (\sigma_{22} + \sigma_{33} < 0) \qquad (7)$$

$$F_{\mathrm{m}}^{\mathrm{c}} = \left[\left(\frac{X_{2c}}{2S_{23}}\right)^2 - 1\right]\frac{(\sigma_{22} + \sigma_{33})}{X_{2c}} + \frac{(\sigma_{22} + \sigma_{33})^2}{4S_{23}^2} + \frac{(\sigma_{23}^2 - \sigma_{22}\sigma_{33})}{S_{23}^2} + \frac{\sigma_{12}^2 + \sigma_{13}^2}{S_{12}^2},\ d_{mc} = 1$$

where X_{1t}, X_{1c}, X_{2t}, X_{2c}, S_{12}, S_{13} and S_{23} are the various strength components [18] and d_{ft}, d_{fc} ,d_{mt} and d_{mc} are the damage variables associated with the four failure modes.

The response of the material after damage initiation (which describes the rate of degradation

of the material stiffness once the initiation criterion is satisfied) is defined by the following equation:

$$\sigma = C(d) \cdot \varepsilon \tag{8}$$

where *C(d)* is a 6×6 symmetric damaged matrix, whose non-zero terms can be written as:

$$\begin{aligned}
C_{11} &= (1-d_f)E_1(1-\nu_{23}\nu_{32})\Gamma \\
C_{22} &= (1-d_f)(1-d_m)E_2(1-\nu_{13}\nu_{31})\Gamma \\
C_{33} &= (1-d_f)(1-d_m)E_3(1-\nu_{12}\nu_{21})\Gamma \\
C_{12} &= (1-d_f)(1-d_m)E_1(\nu_{21}+\nu_{31}\nu_{23})\Gamma \\
C_{23} &= (1-d_f)(1-d_m)E_2(\nu_{32}+\nu_{12}\nu_{31})\Gamma \\
C_{13} &= (1-d_f)(1-d_m)E_1(\nu_{31}+\nu_{21}\nu_{32})\Gamma \\
C_{44} &= (1-d_f)(1-s_{mt}d_{mt})(1-s_{mc}d_{mc})G_{12} \\
C_{55} &= (1-d_f)(1-s_{mt}d_{mt})(1-s_{mc}d_{mc})G_{23} \\
C_{66} &= (1-d_f)(1-s_{mt}d_{mt})(1-s_{mc}d_{mc})G_{13}
\end{aligned} \tag{9}$$

where the global fibre and matrix damage variables as well as the constant Γ are also defined as:

$$\begin{aligned}
d_f &= 1-(1-d_{ft})(1-d_{fc}) \\
d_m &= 1-(1-d_{mt})(1-d_{mc}) \\
\Gamma &= 1/(1-\nu_{12}\nu_{21}-\nu_{23}\nu_{32}-\nu_{13}\nu_{31}-2\nu_{21}\nu_{32}\nu_{13})
\end{aligned} \tag{10}$$

where E_i is the Young's modulus in the *i* direction, G_{ij} is the shear modulus in the *i-j* plane and ν_{ij} is the Poisson's ratio for transverse strain in the *j*-direction, when the stress is applied in the *i*-direction. The Young's moduli, shear's moduli, Poisson's ratios and strengths of the GFPP are given in Table 3.

The factors s_{mt} and s_{mc} in the definitions of the shear moduli are introduced to control the reduction in shear stiffness caused by tensile and compressive failure in the matrix respectively. The following values are recommended in ABAQUS [22]: $s_{mt} = 0.9$ and $s_{mc} = 0.5$.

3.2.2 Strain-rate effects in the mechanical properties

The effects of strain-rate on the mechanical properties of a composite material are typically

modelled using strain-rate dependent functions for both the elastic modulus and the strength. Yen [23] developed logarithmic functions to account for strain-rate effects in a composite material as follows:

$$\begin{aligned}\{S_{RT}\} &= \{S_0\}\left(1 + C_1 \ln \frac{\dot{\bar{\varepsilon}}}{\dot{\varepsilon}_0}\right) \\ \{E_{RT}\} &= \{E_0\}\left(1 + C_2 \ln \frac{\dot{\bar{\varepsilon}}}{\dot{\varepsilon}_0}\right)\end{aligned} \tag{11}$$

where:

$$\begin{aligned}\{\dot{\bar{\varepsilon}}\} &= \{|\dot{\varepsilon}_1| \quad |\dot{\varepsilon}_2| \quad |\dot{\varepsilon}_1| \quad |\dot{\varepsilon}_2| \quad |\dot{\varepsilon}_{12}| \quad |\dot{\varepsilon}_{13}| \quad |\dot{\varepsilon}_{23}|\}^T \\ \{S_{RT}\} &= \{X_{1t} \quad X_{2t} \quad X_{1c} \quad X_{2c} \quad S_{12} \quad S_{13} \quad S_{23}\}^T \\ \{E_{RT}\} &= \{E_1 \quad E_2 \quad E_3 \quad G_{12} \quad G_{13} \quad G_{23}\}^T\end{aligned} \tag{12}$$

and the subscript '*RT*' refers to the rate-adjusted values, the subscript '0' refers to the static value, $\dot{\varepsilon}_0 = 1\text{s}^{-1}$ is the reference strain-rate, $\dot{\bar{\varepsilon}}$ is the effective strain-rate, C_1 and C_2 are the strain-rate constants, respectively.

3.2.3 Implementation of the material model in ABAQUS/Explicit

The material model and failure criteria described in the previous sections were implemented in ABAQUS/Explicit using the VUMAT subroutine. This subroutine is compiled and enables ABAQUS/Explicit to obtain the required information regarding the state of the material and the material mechanical response during each time step, at each integration point of each element. The stresses are computed within the VUMAT subroutine using the given strains and the material stiffness coefficients. Based on these stresses, Hashin's 3D failure criteria outlined in Eq.(7) are calculated, and the elastic modulus and strength values are adjusted for strain-rate effects using Eq.(11). When an element fails, as determined by the failure criteria, the element status is then changed from 1 to 0. At this point, the stresses at that material point are reduced to zero and it no longer contributes to the model stiffness. When all of the

material status points of an element have been reduced to zero, the element is removed from the mesh.

3.3 Cohesive elements and material properties

Debonding at the interface between the composite and aluminium layers was modelled using cohesive elements available in ABAQUS [22]. The elastic response was defined in terms of a traction-separation law with uncoupled behaviour between the normal and shear components. The default choice of the constitutive thickness for modeling the response, in terms of traction versus separation, is 1.0, regardless of the actual thickness of the cohesive layer. Thus, the diagonal terms in the elasticity matrix and density should be calculated using the true thickness of the cohesive layer as follows:

$$K_{nn} = \frac{E_n}{t_c}; \quad K_{ss} = \frac{E_s}{t_c}; \quad K_{tt} = \frac{E_t}{t_c}$$
$$\rho = \rho_c t_c \tag{13}$$

The quadratic nominal stress and energy criterion were used to model damage initiation and damage evolution, respectively. Damage initiated when a quadratic interaction function, involving the nominal stress ratios, reached unity. Damage evolution was defined based on the energy conjunction with a linear softening law. The mechanical properties of the cohesive elements were obtained from Karagiozova et al. [16] and are given in Table 4.

4. Finite Element Modelling

The 3D FML panel consisted of the aluminium alloy, the composite and the cohesive layers as three separate parts. The aluminium and composite layers were meshed using C3D8R elements, which are eight-noded, linear hexahedral elements with reduced integration and hourglass control. The interfaces between the aluminium and the composite layers were created using eight-node 3D cohesive elements (COH3D8). As the structure has symmetry in both the directions, only a quarter of each FML panel was modeled with the appropriate

boundary conditions applied along the planes of symmetry, as shown in Figure 1. A mesh size of 1×1 mm for a central area of 60×60 mm (Figure 1) was found to be the most appropriate for these FML panels. Symmetric boundary conditions were applied to the nodes lying on the XY and YZ planes, while the other two edges were fully fixed. The general contact algorithm was used for the definition of contact between the two neighbouring layers of the aluminum and the composite. Detailed finite element modelling can be found in the paper by Vo, et al. [17].

5. Results and Discussion

Since there are no experimental data available in the literature to describe strain-rate effects in the woven glass-fibre/polypropylene composite, rate-dependent material models, with different values of the strain-rate constant, were investigated in this study. A material model incorporating strain-rate effects in the strength, shear and the through-thickness modulus values was chosen. Strain-rate constant values that agreed well with the experimental results were $C_1 = C_2 = 0.35$. This material model is consistent with results of McCarthy et al. [24] and Gama and Gillespie [25]. In their research, strain-rate effects were not taken into account for the in-plane elastic moduli E_1 and E_2 of the composite layers. Initially, two FML panels, A3T24-8 and A4T34-5, were studied to investigate their transient and residual displacements. After conducting a number of convergence studies, numerical simulations were carried out over a time period of 4 ms. The transient displacement relates to the first peak in the displacement time trace and the residual displacement is taken as the average after more than three cycles following unloading. The variation of the front and back displacements with time are shown in Figure 2. Here, the highly dynamic response of the panels is clearly evident with the displacements oscillating significantly in response to the blast event. As expected, the deflections of the thinner A3T24 panel are greater than those of its stiffer A4T34 counterpart. It is worth noting that the difference between the front and back surface displacements is

greater than the initial thickness of the panel. This increase in the effective thickness of the FML is associated with the opening up of planes of delamination within the volume of the laminate. Due to the relatively low impulse, there is a large elastic oscillation regime in the dynamic response of these panels. FE models of other types of FML panels subjected to a low impulse were also developed to broaden the validation. The experimental and numerical results are presented in Table 5. Reasonable agreement between the predicted and experimental mid-point displacements is observed. Closer examination of data suggests that the model tends to under-estimate the front surface displacement and over-estimate the back surface deformation of the targets. There are large differences between the back face and the front face displacements, which indicate the interfacial failure. Comparing the experimental and numerical failure modes of five typical panels, as shown in Figure 3, the simulations accurately capture the primary failure mechanisms in the FMLs, which include large out-of-plane plastic displacements, debonding of the back face and local buckling of the internal aluminium layer.

The numerical results corresponding to FML panels based on the four aluminium alloys are presented in Table 6. It can be seen that the front and back displacements of those panels based on the aluminium 7075-T6 are the smallest, whereas those based on the aluminium 2024-O are the largest. This suggests that the properties of the aluminium alloy, most particularly its yield stress, greatly influence the blast response of these hybrid materials. The 4/3 A4T32-4 panel was chosen to investigate the transient response, deformed shapes and energy histories of four types of panel. Figure 4 shows comparisons of the variation of the front and back displacements with time. The deformed shapes of the A4T32-4 panel based on the four aluminium alloys are shown in Figure 5. It can be seen that the permanent displacements tend to decrease with increasing yield strength of the aluminium alloy, as shown in Figure 6. In this case, the permanent displacement of the A4T32 panel based on the 2024-O alloy is almost double that of the aluminium 7075-T6. Figure 7 shows the variation of

the energy dissipated in debonding with the yield strength of the aluminium alloy. From the figure, it is evident that this energy increases with the properties of the alloy, supporting the observations in Figure 5 which suggest that the debonding area also increases with σ_y. Since there is no splitting damage in the composite material, and assuming that the energy associated with delaminating the composite layers is negligible, the energy balance using the total energy quantities computed by ABAQUS is given by:

$$E_{TOTAL} = IE_{ALL} + KE_{ALL} - WK_{ALL} = \text{constant} \quad (14)$$

where KE_{ALL} is the kinetic energy, WK_{ALL} is the external work and IE_{ALL} is the total internal energy, defined by:

$$IE_{ALL} = SE_{ALL} + PD_{ALL} + ED_{ALL} + AE_{ALL} \quad (15)$$

where SE_{ALL} is the recoverable strain energy, PD_{ALL} is the plastic dissipation energy, ED_{ALL} is the energy dissipated by debonding and AE_{ALL} is the artificial strain energy.

The time histories of the kinetic (KE_{ALL}) and the total internal energies (IE_{ALL}) for the four cases were determined and are shown in Figure 8. As E_{TOTAL} remains constant, the energy balance is clearly maintained throughout the analysis. The kinetic energy (KE_{ALL}) increases and reaches a maximum value at an early stage of the blast event, and then, decreases. In contrast, the internal energy (IE_{ALL}) increases from zero and exhibits small oscillations, before reaching a maximum value. The external work (WK_{ALL}) and the components of the total internal energy (IE_{ALL}) are presented in Figure 9. Here, the 'artificial energy' (AE_{ALL}) is the energy associated with the application of hourglass control in ABAQUS, which prevents excessive distortion of the mesh. It can be seen that the 'artificial energy' (AE_{ALL}) is significantly lower than the internal energy (IE_{ALL}), indicating that the solution is trustworthy ([22]). Figure 9 also indicates that most of the work done by the blast load is dissipated in plastic deformation of the aluminium alloy and debonding of the composite and metal layers.

Debonding of the cohesive layer absorbs a small proportion of the blast energy, relative to the energy dissipated in plastically deforming the aluminium. It can be seen that for a given impulse, the FML based on the 2024-O alloy absorbs the greatest amount of energy in plastic deformation. It is worth noting, however, that the energy dissipated in plastic deformation of the alloy decreases as its yield strength increases. Here, this additional available energy is absorbed in debonding the composite and metal layers, as previously observed in Figure 7. This suggests that introducing an alloy with a higher yield strength allows for greater out-of-plane elastic deformations during the blast event (the yield strain will be higher). As these elastic displacements increase, the interfaces between the composite and metal layers are likely to fracture, leading to debonding between the constituent materials. This may explain why the levels of debonding are greater in the higher strength alloys.

In an attempt to compare FML panels based on different aluminium alloys, the most appropriate way to do this is by employing the dimensionless analysis used by Langdon et al. ([9], [26]). Here, the dimensionless impulse and displacements are given by:

$$\begin{aligned} \Phi_q &= \frac{I\left(1+\ln\frac{BL}{\pi r_0^2}\right)}{2t^2\sqrt{BL\rho\sigma_{UTS}}} \\ \delta_B &= \frac{d_B}{t} \end{aligned} \tag{16}$$

where ρ is the material density, B, L are the plate width and length dimensions, t is the plate thickness and σ_{UTS}: effective ultimate tensile strength. Reyes and Cantwell [6] showed that the tensile strength of FMLs can be approximated using the rule of mixtures by using:

$$\sigma_{UTS} = \frac{\left(\sigma_{UTS_{Al}} t_{Al} + \sigma_{UTS_{com}} t_{com}\right)}{t} \tag{17}$$

Using the constituent properties of the aluminium alloy in Table 2, the effective ultimate tensile strength values were calculated and are given in Table 7.

The dimensionless back displacements of the FML panels are given in Table 6 and plotted against the dimensionless impulse in Figure 10. As expected, there is a reasonably linear relationship between the dimensionless back displacement and the dimensionless impulse for the FMLs based on the four types of aluminium alloy. Clearly, there is some scatter in the data, which is due to the difference in stacking sequences and thicknesses between the different FMLs, especially for A5T42 that consists of five aluminium layers and four composite layers. The equation for dimensionless impulse assumes that the yield stress obeys a rule of mixtures approach. This applies in tension but is less accurate in bending. Changing the thickness and the stacking sequence will lead to errors associated with the limitations related to this rule of mixtures approach. In addition, Eq. (17) applies to the in-plane properties of the FMLs, rather than their flexural behaviour. Figure 10 highlights the influence of the properties of the aluminium alloy on the blast resistance of FMLs. The trend-lines are almost parallel to each other, with the uppermost line corresponding to the FML based on the 2024-O alloy and the lowest to the 7075-T6 FML. The trend-line equations for the back face dimensionless displacements are given by:

$$\begin{aligned}
&\text{Aluminium 2024-O: } \delta_B = 0.80\Phi_q + 0.87, R^2 = 0.90 \\
&\text{Aluminium 2024-T3: } \delta_B = 0.76\Phi_q + 0.52, R^2 = 0.93 \\
&\text{Aluminium 6061-T6: } \delta_B = 0.79\Phi_q + 0.63, R^2 = 0.94 \\
&\text{Aluminium 7075-T6: } \delta_B = 0.64\Phi_q + 0.35, R^2 = 0.82
\end{aligned} \tag{18}$$

6. Conclusions

A parametric study of the low-impulse blast behaviour of FMLs based on different aluminium alloys is presented. Here, three dimensional finite element models of FML panels based on a 2024-O aluminium alloy and a woven glass-fibre/polypropylene composite subjected to low-impulse localised blast loading are developed and validated against previously-published

experimental data. Hashin's 3D failure criteria, incorporating strain-rate effects in the GFPP is implemented into ABAQUS/Explicit. Using the validated models, a parametric study is used to investigate the influence of the properties of the aluminium alloy on the blast resistance of FMLs based on the four aluminium alloys, namely 2024-O, 2024-T3, 6061-T6 and 7075-T6. The residual back displacement of the FML panels decreases with the increasing yield strength of the aluminium alloy. Using a dimensionless analysis procedure, it has been shown that there is an approximate linear relationship between the dimensionless back surface displacement and the dimensionless impulse for all aluminium alloys investigated here. However, changing the thickness and the stacking sequence is likely lead to errors associated with the limitations related to this rule of mixtures approach. It has also been shown that the level of debonding is strongly dependent on the yield characteristics of the aluminium alloy. Given that the aluminium alloy does not rupture in these analyses, the failure strain is not influencing the response of the panels. The elastic moduli of the alloys are all similar so that this is not considered to be an important parameter in this investigation. The evidence suggests that the 7075-T6 alloy offers the best resistance to blast loading of the laminates considered.

7. Acknowledgments

The authors would like to thank the Leverhulme Trust for the financially supporting the work presented in this paper. The authors also would like to acknowledge the use of the UK

National Grid Service in carrying out this work.

8. References

[1] A. Vlot, Impact loading on fibre metal laminates, International Journal of Impact Engineering 18 (3) (1996) 291 – 307.

[2] S. Krishnakumar, Fibre metal laminates-the synthesis of metals and composites, Materials and Manufacturing Processes 9 (2) (1994) 295–354.

[3] L. B. Vogelesang, A. Vlot, Development of fibre metal laminates for advanced aerospace structures, Journal of Materials Processing Technology 103 (1) (2000) 1 – 5.

[4] P. Compston, W. J. Cantwell, C. Jones, N. Jones, Impact perforation resistance and fracture mechanisms of a thermoplastic based fiber-metal laminate, Journal of Materials Science Letters 20 (2001) 597–599.

[5] G. Reyes-Villanueva, W. J. Cantwell, The high velocity impact response of composite and FML-reinforced sandwich structures, Composites Science and Technology 64 (1) (2004) 35 – 54.

[6] G. Reyes, W. J. Cantwell, The mechanical properties of fibre-metal laminates based on glass fibre reinforced polypropylene, Composites Science and Technology 60 (7) (2000) 1085 – 1094.

[7] H. J. Fleisher, Design and explosive testing of a blast resistant luggage container, in: International conference on structures under shock and impact, 1996, pp. 51–60.

[8] G. S. Langdon, S. L. Lemanski, G. N. Nurick, M. C. Simmons, W. J. Cantwell, G. K. Schleyer, Behaviour of fibre-metal laminates subjected to localised blast loading: Part I–

Experimental observations, International Journal of Impact Engineering 34 (7) (2007) 1202 – 1222.

[9] S. L. Lemanski, G. N. Nurick, G. S. Langdon, M. C. Simmons, W. J. Cantwell, G. K. Schleyer, Behaviour of fibre metal laminates subjected to localised blast loading–Part II: Quantitative analysis, International Journal of Impact Engineering 34 (7) (2007) 1223 – 1245.

[10] G. S. Langdon, G. N. Nurick, S. L. Lemanski, M. C. Simmons, W. J. Cantwell, G. K. Schleyer, Failure characterisation of blast-loaded fibre-metal laminate panels based on aluminium and glass-fibre reinforced polypropylene, Composites Science and Technology 67 (7-8) (2007) 1385 – 1405.

[11] G. S. Langdon, W. J. Cantwell, G. N. Nurick, Localised blast loading of fibre-metal laminates with a polyamide matrix, Composites Part B: Engineering 38 (7-8) (2007) 902 – 913.

[12] G. S. Langdon, Y. Chi, G. N. Nurick, P. Haupt, Response of GLARE© panels to blast loading, Engineering Structures 31 (12) (2009) 3116 – 3120.

[13] T. Kotzakolios, D. Vlachos, V. Kostopoulos, Investigation of blast response of GLARE laminates: comparison against experimental results, Plastics, Rubber and Composites 40 (6-7) (2011) 349 – 355.

[14] T. Kotzakolios, D. Vlachos, V. Kostopoulos, Blast response of metal composite laminate fuselage structures using finite element modelling, Composite Structures 93 (2) (2011) 665 – 681.

[15] C. Soutis, G. Mohamed, A. Hodzic, Modelling the structural response of glare panels to blast load, Composite Structures 94 (1) (2011) 267 – 276.

[16] D. Karagiozova, G. S. Langdon, G. N. Nurick, S. C. K. Yuen, Simulation of the response of fibre-metal laminates to localised blast loading, International Journal of Impact Engineering 37 (6) (2010) 766 – 782.

[17] T.P. Vo, Z. W. Guan, W. J. Cantwell and G. K. Schleyer, Low-impulse blast behaviour of fibre-metal laminates, Composite Structures 94 (3) (2012) 954-965.[18]

[18] Z. Hashin, Failure criteria for unidirectional fiber composites, Journal of Applied Mechanics 47 (1980) 329–334.

[19] G. S. Langdon, Yuen, S. C. K. Yuen and G. N. Nurick, Experimental and numerical studies on the response of quadrangular stiffened plates. Part II: localised blast loading, International Journal of Impact Engineering 31(1) (2005) 85 - 111

[20] D. Karagiozova, G. N. Nurick and G. S. Langdon, Behaviour of sandwich panels subject to intense air blasts - Part 2: Numerical simulation, Composite Structures, 2009, 91 (4), 442 – 450

[21] C. N. Kingery, G. Bulmash and U. A. B. R. Laboratory, Air blast parameters from TNT spherical air burst and hemispherical surface burst, Ballistic Research Laboratories, 1984.

[22] ABAQUS, Theory Manual, Version 6.9, Hibbitt, Karlsson & Sorensen, Inc. (2009).

[23] C. F. Yen, Ballistic impact modeling of composite materials, in: Proceedings of the 7th International LS-DYNA Users Conference, Vol. 6, 2002, pp. 15–23.

[24] M. A. McCarthy, J. R. Xiao, N. Petrinic, A. Kamoulakos, V. Melito, Modelling of bird strike on an aircraft wing leading edge made from fibre metal laminates- part 1: Material modelling, Applied Composite Materials 11 (2004) 295–315.

[25] B. A. Gama, J. W. Gillespie Jr., Finite element modeling of impact, damage evolution and penetration of thick-section composites, International Journal of Impact Engineering 38 (4) (2011) 181 – 197.

[26] G. S. Langdon, W. J. Cantwell, G. N. Nurick, The blast response of novel thermoplastic-based fibre-metal laminates - some preliminary results and observations, Composites Science and Technology 65 (6) (2005) 861 – 872.

[27] D. R. Lesuer, Experimental Investigations of Material Models for Ti-6Al-4V Titanium and 2024-T3 Aluminum, Tech. rep., Lawrence Livermore National Laboratory, Livermore, CA. (2000).

[28] B. Corbett, Numerical simulations of target hole diameters for hypervelocity impacts into elevated and room temperature bumpers, International Journal of Impact Engineering 33 (1-12) (2006) 431 – 440.

[29] N. S. Brar, V. S. Joshi, B. W. Harris, Constitutive model constants for Al7075-T651 and Al7075-T6, AIP Conference Proceedings 1195 (1) (2009) 945–948.

CAPTIONS OF FIGURES

Figure 1: Dimensions, loading, boundary conditions and mesh generation for typical 3/2 FML panel.

Figure 2: Back and front face displacements versus time for panels A3T24-8 and A4T34-5.

Figure 3: Comparison between the experiments and numerical simulations for five FML panel s.

Figure 4: Back and front face displacements versus time for the A4T32-4 panel based on the four aluminium alloys.

Figure 5: Deformed shapes of the A4T32-4 panel based on the four aluminium alloys.

Figure 6: Residual front and back face displacements of the A4T32-4 panel based on the four aluminium alloys versus yield strength.

Figure 7: Debonding energy of the A4T32-4 panel based on the four aluminium alloys versus yield strength.

Figure 8: The time history of total internal energy and kinetic energy of the A4T32-4 panel based on the four aluminium alloys.

Figure 9: External work and total internal energy components (PD, SE, ED and AE) of the A 4T32-4 panel based on the four aluminium alloys.

Figure 10: Graph of dimensionless permanent displacement of back face versus dimensionless impulse.

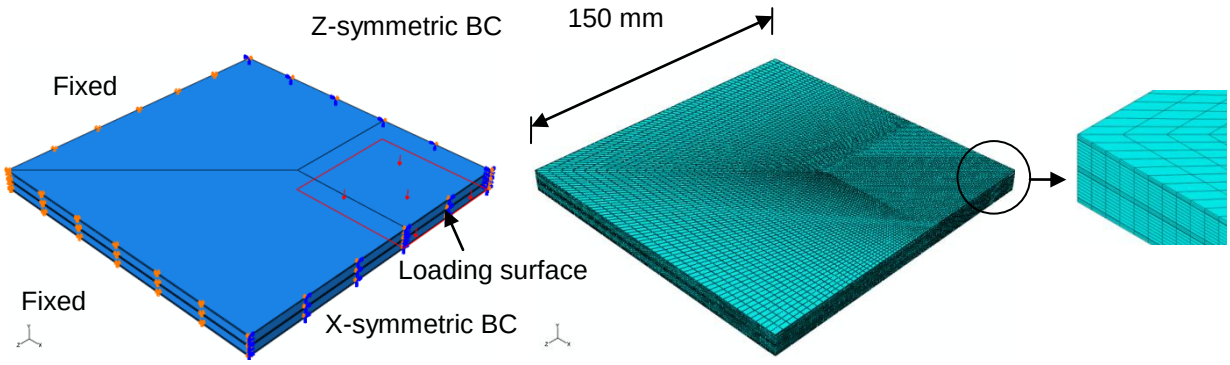

Figure 1: Dimensions, loading, boundary conditions and mesh generation for typical 3/2 FML panel.

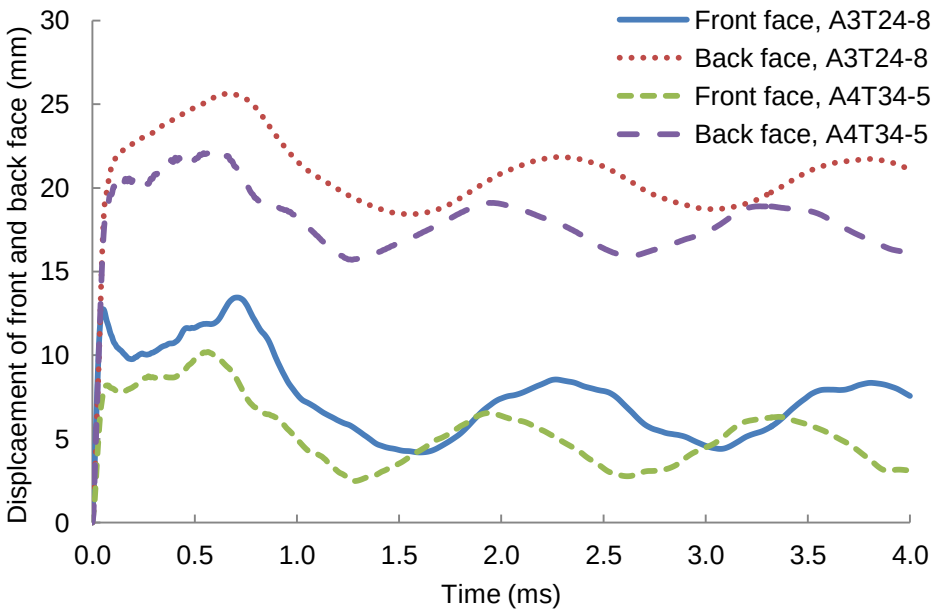

Figure 2: Back and front face displacements versus time for panels A3T24-8 and A4T34-5.

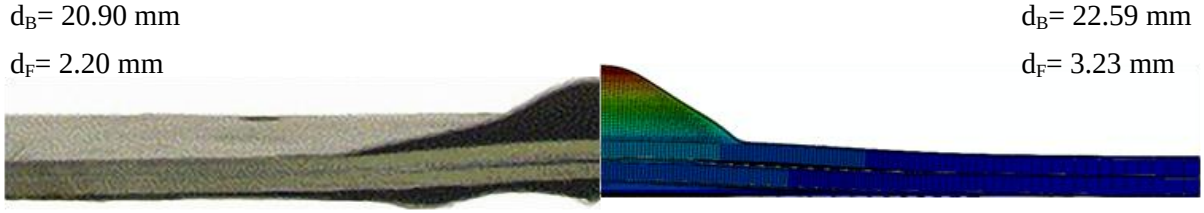

a. A3T28-5, I=10.34 Ns

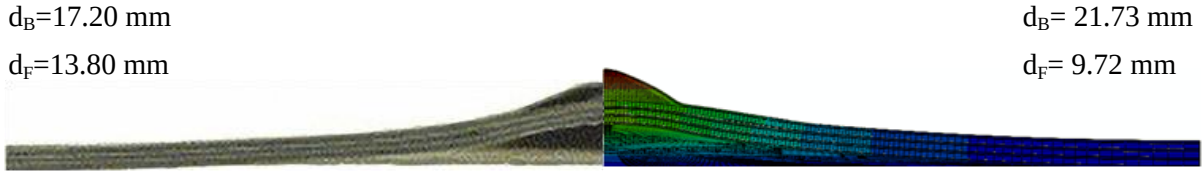

b. A4T32-4, I=7.23 Ns

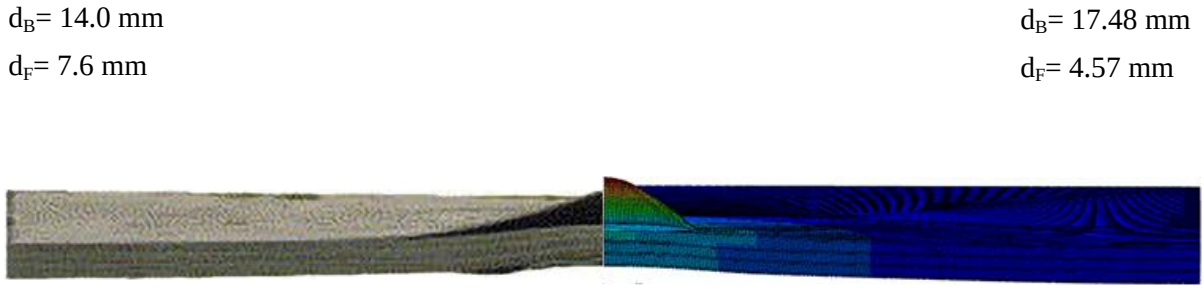

c. A4T34-5, I=7.01 Ns

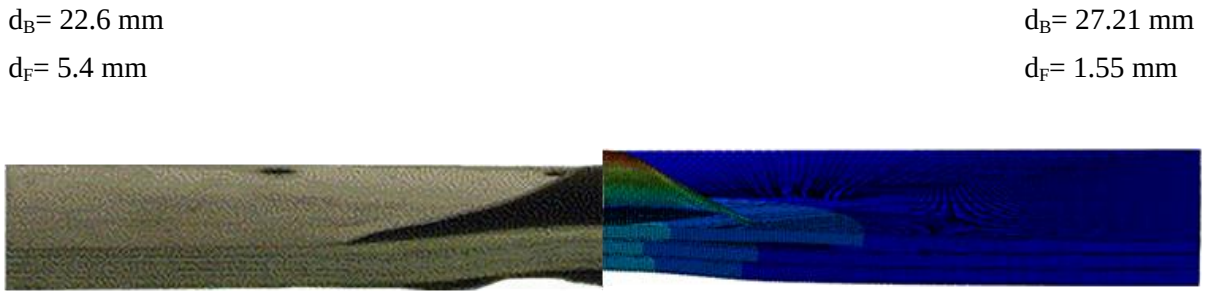

d. A4T36-2, I=11.61 Ns

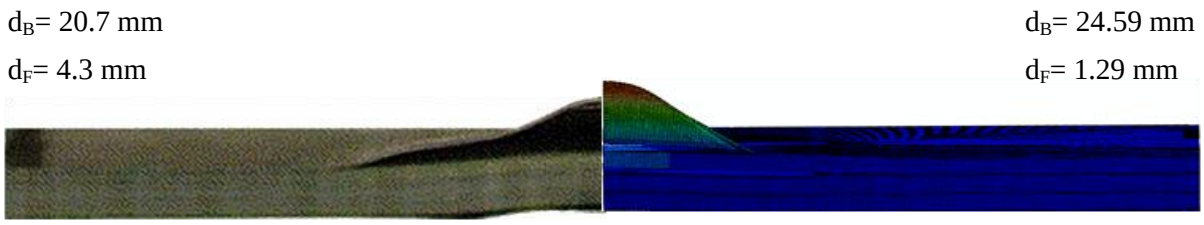

e. A4T38-2, I=11.13 Ns

Figure 3: Comparison between the experiments and numerical simulations for five FML panels.

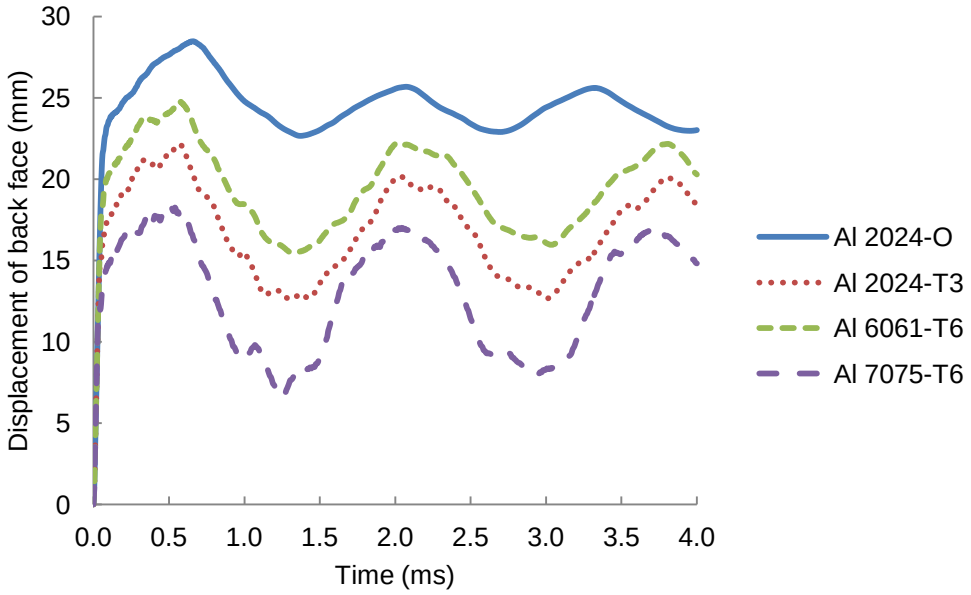

a. Back displacement

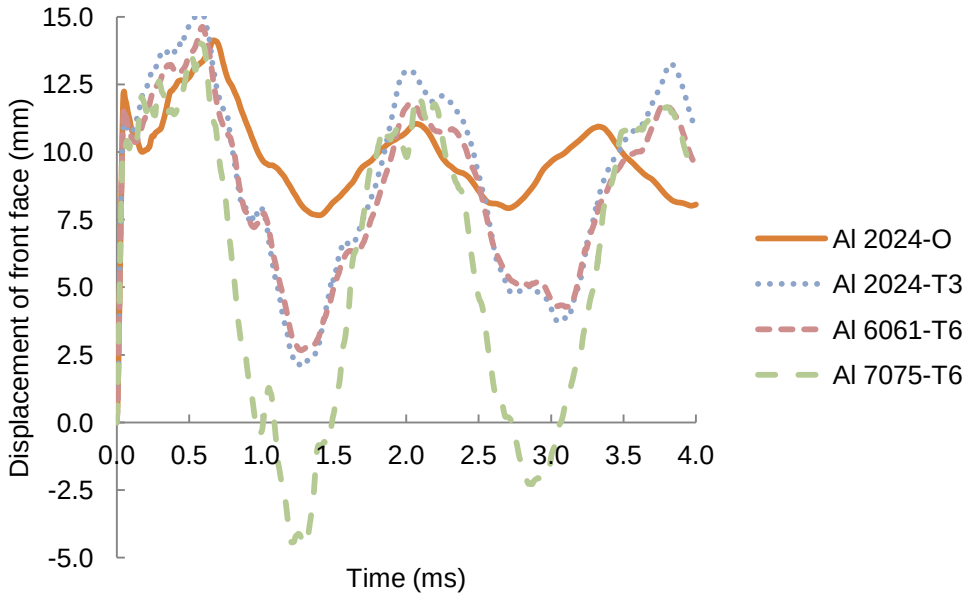

b. Front displacement

Figure 4: Back and front face displacements versus time for the A4T32-4 panel based on the four aluminium alloys.

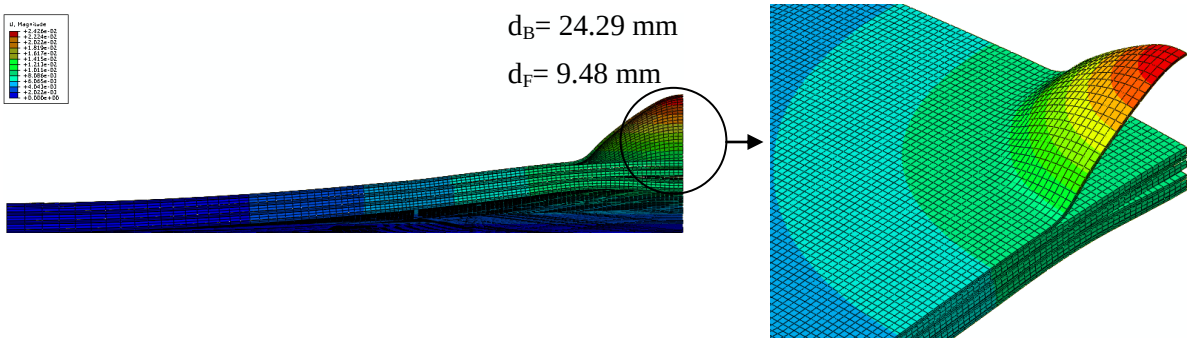

a. Al 2024-O

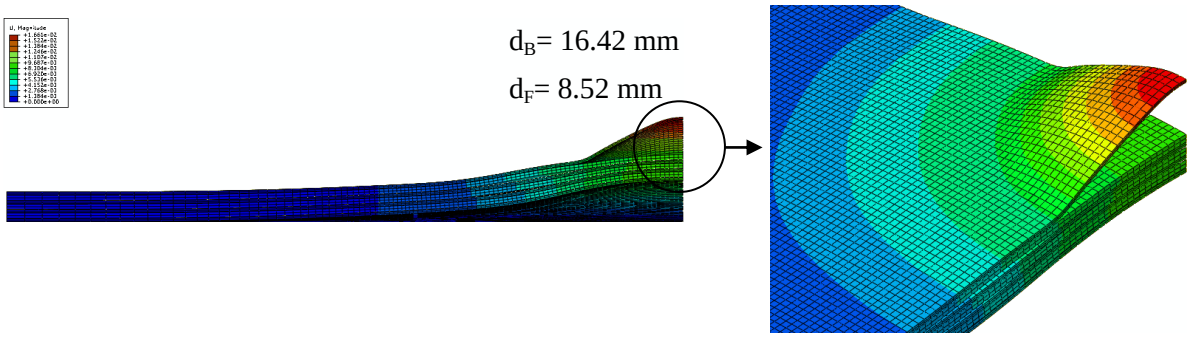

b. Al 2024-T3

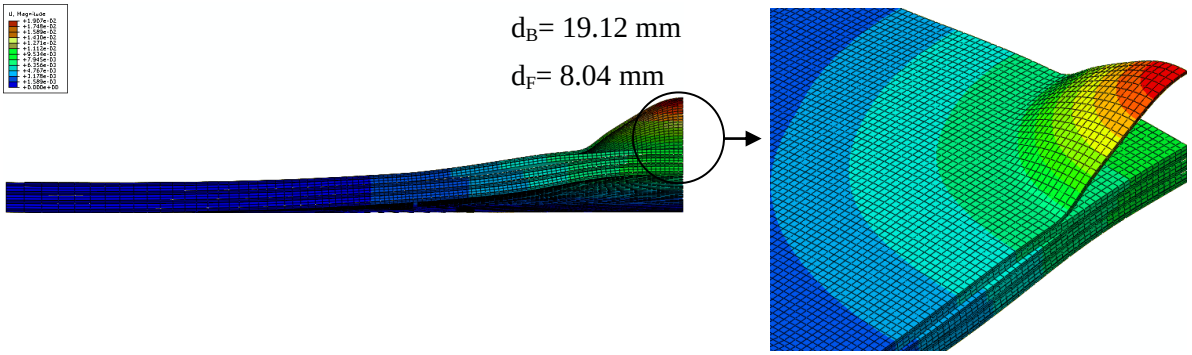

c. Al 6061-T6

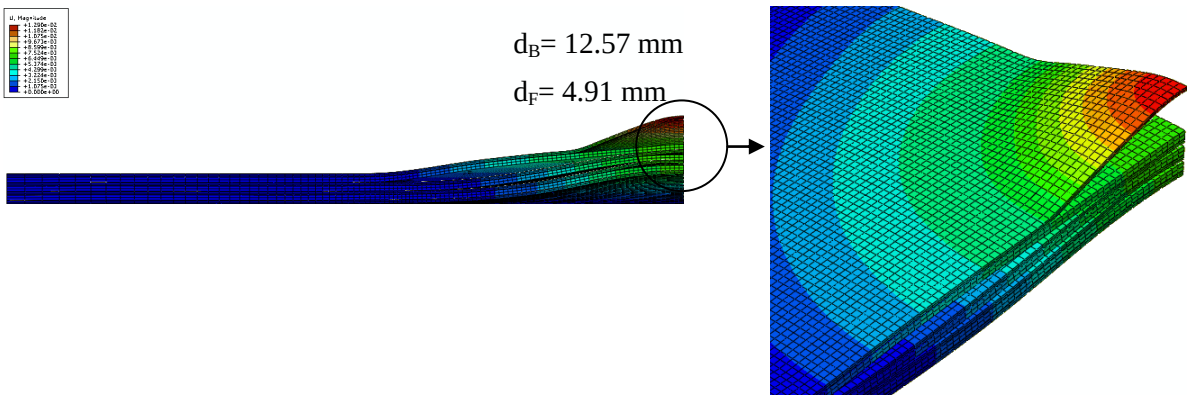

d. Al 7075-T6

Figure 5: Deformed shapes of the A4T32-4 panel based on the four aluminium alloys.

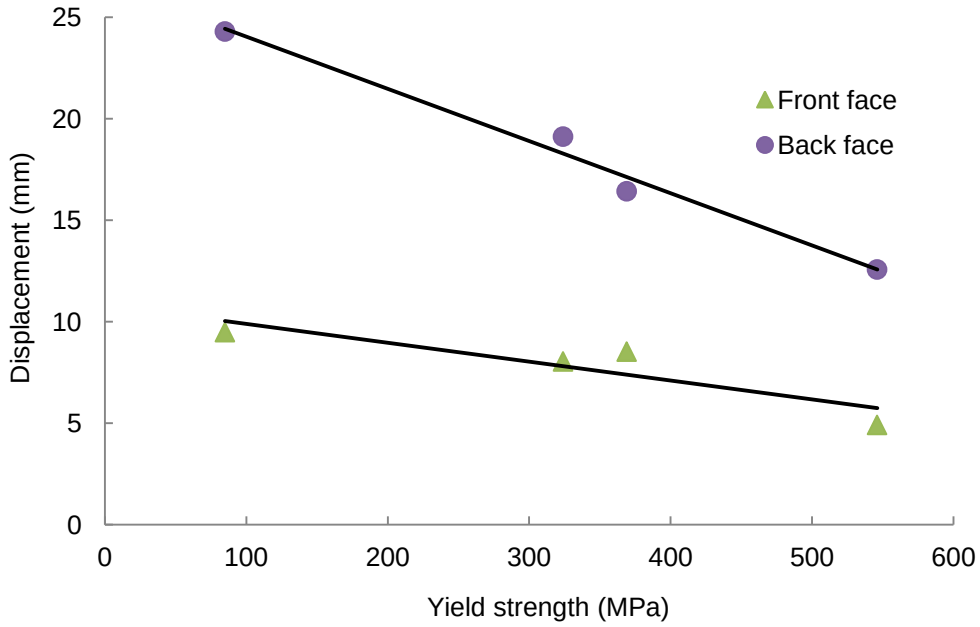

Figure 6: Residual front and back face displacements of the A4T32-4 panel based on the four aluminium alloys versus yield strength.

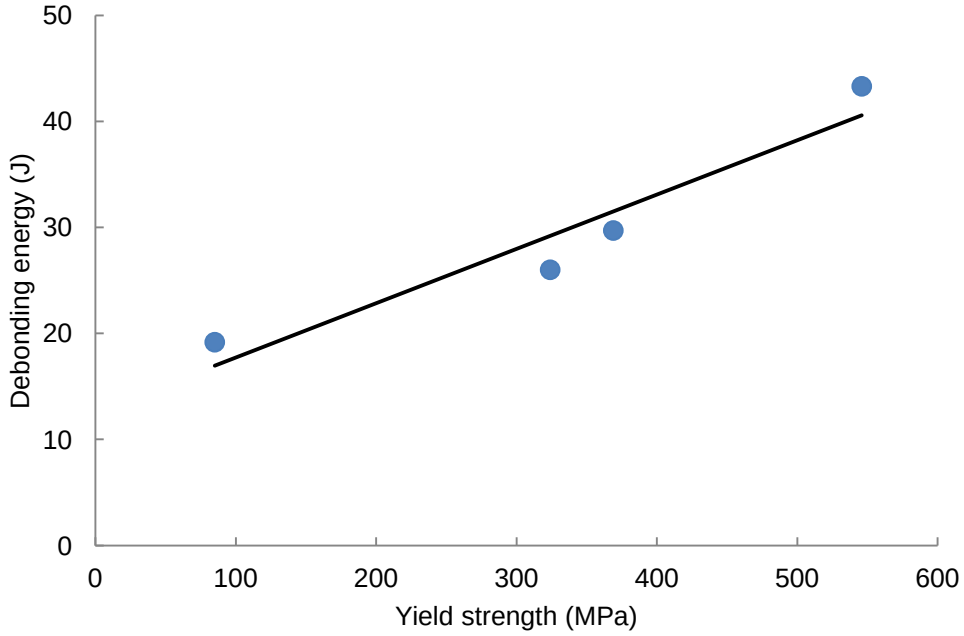

Figure 7: Debonding energy of the A4T32-4 panel based on the four aluminium alloys versus yield strength.

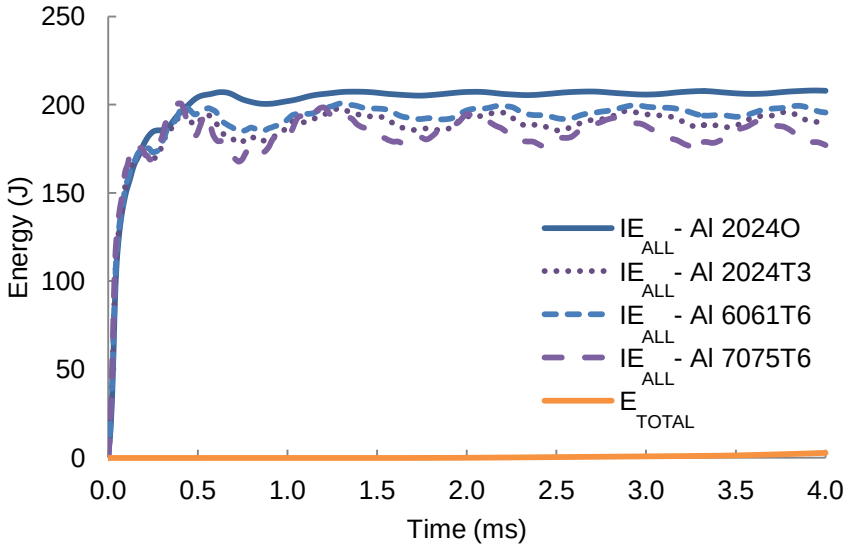

a. Total internal energy (IE_{ALL}) and E_{TOTAL}

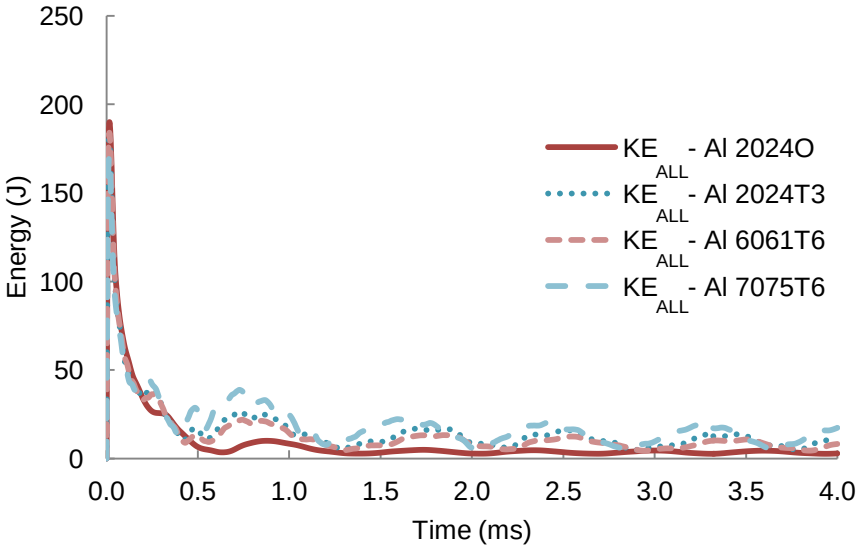

b. Kinetic energy (KE_{ALL}).

Figure 8: The time history of total internal energy and kinetic energy of the A4T32-4 panel based on the four aluminium alloys.

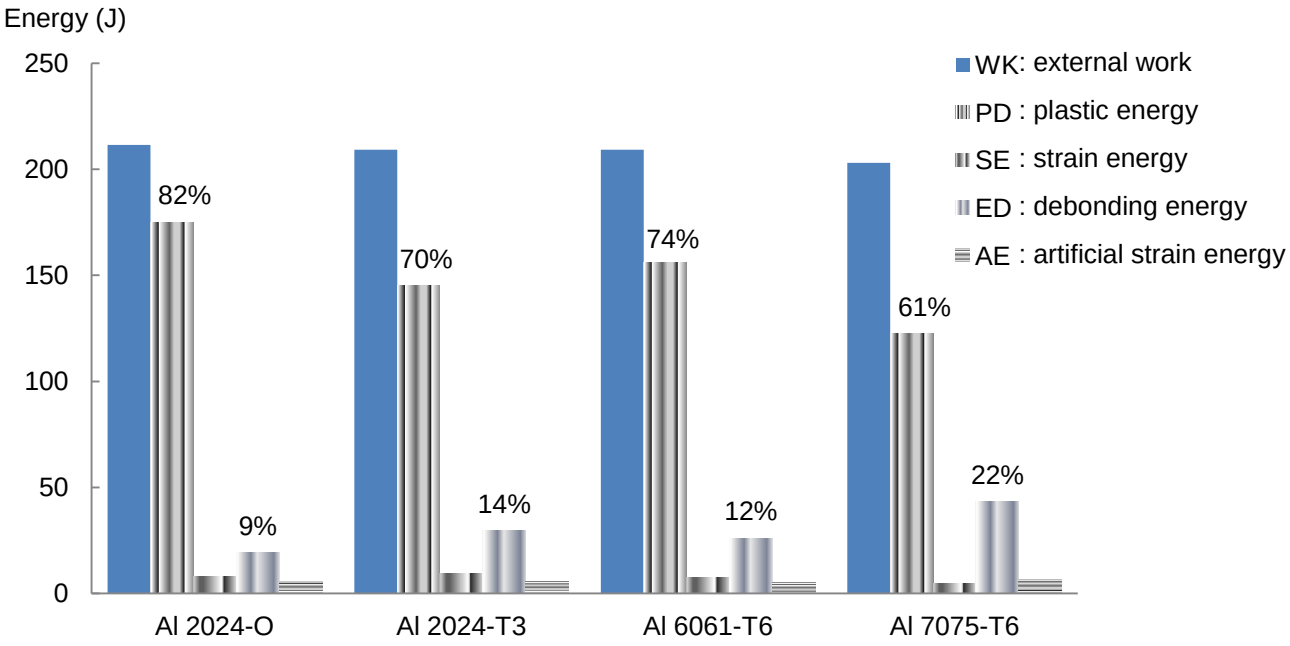

Figure 9: External work and total internal energy components (PD, SE, ED and AE) of the A4T32-4 panel based on the four aluminium alloys.

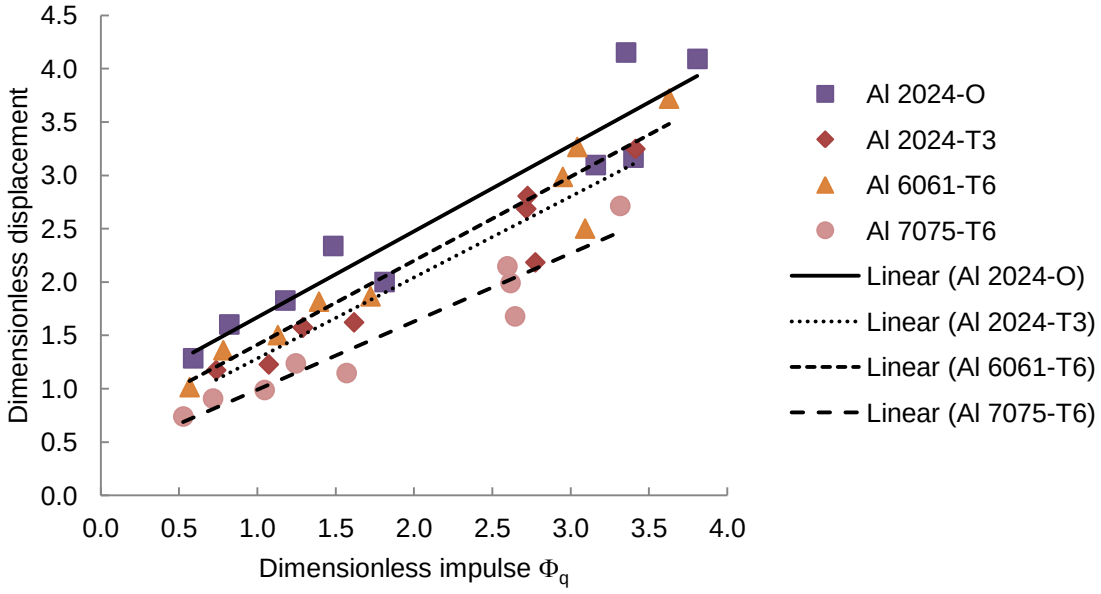

Figure 10: Graph of dimensionless permanent displacement of back face versus dimensionless impulse.

List of Tables

Table 1: Details of the lay-ups and impulses for verification.

Lay-ups	No. of layers	Thickness (mm)	Impulse (Ns)
A2T18-4	10	5.60	7.94
A3T24-8	11	6.06	7.85
A3T26-3	15	8.10	9.54
A3T28-5	19	9.82	10.34
A4T32-4	10	5.85	7.23
A4T34-5	16	8.73	7.01
A4T36-2	22	11.48	11.61
A4T38-2	28	13.90	11.13
A5T42-4	13	7.46	8.87

Table 2: Johnson-Cook constants and static tensile strength for aluminium alloys.

Aluminium type	A (MPa)	B (MPa)	n	C	D_1	D_2	D_3	D_4	Ultimate tensile strength (MPa)
Al 2024-O [16]	85	325	0.40	0.0083	0.130*	0.130*	-1.500*	0.011*	186
Al 2024-T3 [27]	369	684	0.73	0.0083	0.130	0.130	-1.500	0.011	483
Al 6061-T6 [28]	324	114	0.42	0.0020	-0.770	1.450	-0.470	0.000	310
Al 7075-T6 [29]	546	678	0.71	0.0240	-0.068	0.451	-0.952	0.036	572

* Damage constants for Al 2024-T3 were used due to the lack of available data.

Table 3: Properties of the GFPP layers.

Elastic properties	Values	Progressive failure	Values
ρ (kg/m^3)	1800	X_{1t} (MPa)	300
E_1 (GPa)	13.0	X_{1c} (MPa)	200
E_2 (GPa)	13.0	X_{2t} (MPa)	300
E_3 (GPa)	2.40	X_{2c} (MPa)	200
G_{12} (GPa)	1.72	S_{12} (MPa)	140
G_{13} (GPa)	1.72	S_{13} (MPa)	140
G_{23} (GPa)	1.69	S_{23} (MPa)	140
ν_{12}	0.1		
ν_{13}	0.3		
ν_{23}	0.3		

Table 4: Properties of the cohesive layers.

Elastic properties					Damage initiation		Damage evolution			
Thickness t_c (m)	ρ_c (kg/m^3)	E_n (GPa)	E_s (GPa)	E_t (GPa)	t_n^0 (MPa)	t_s^0 (MPa)	t_t^0 (MPa)	G_n^c (J/m^2)	G_s^c (J/m^2)	G_t^c (J/m^2)
10^{-4}	920	2.05	0.72	0.72	140	300	300	2000	3000	3000

G_n^c, G_s^c and G_t^c are the critical fracture energies in the normal, the first, and the second shear directions.

t_n^0, t_s^0 and t_t^0 are the critical nominal normal stress, the first and the second shear stresses.

Table 5: Comparison of experimental data from Ref. [9] and numerical simulation results of transient and permanent displacements of front and back faces for verification.

Panel	Impulse (Ns)	Numerical				Experiment	
		Transient displ. (mm)		Permanent displ. (mm)		Permanent displ. (mm)	
		Front	Back	Front	Back	Front	Back
A2T18-4	7.94	12.86	28.09	4.95	22.19	9.10	16.30
A3T24-8	7.85	13.06	25.65	6.06	20.34	10.10	19.30
A3T26-3	9.54	12.07	26.91	4.32	20.35	7.20	23.70
A3T28-5	10.34	10.56	28.47	3.23	22.59	2.20	20.90
A4T32-4	7.23	13.91	25.79	9.72	21.73	13.80	17.20
A4T34-5	7.01	10.19	22.19	4.57	17.48	7.60	14.00
A4T36-2	11.61	9.30	32.70	1.55	27.21	5.40	22.60
A4T38-2	11.13	6.82	30.43	1.29	24.59	4.30	20.70
A5T42-4	8.87	13.28	30.32	7.95	25.31	11.50	19.90

Table 6: Summary of permanent front and back face displacements of FMLs based on the four aluminium alloys.

Panel	Aluminium types	Dimensional parameters			Dimensionless parameters		
		Impulse (Ns)	Displacement (mm)		Impulse	Front	Back
			Front	Back			
A2T18-4	Al 2024-O	8.00	5.53	22.92	3.81	0.99	4.09
	Al 2024-T3	8.00	5.17	18.19	3.41	0.92	3.25
	Al 6061-T6	8.00	5.71	20.84	3.63	1.02	3.72
	Al 7075-T6	8.00	4.50	15.20	3.32	0.80	2.71
A3T24-8	Al 2024-O	8.00	6.63	18.77	3.16	1.09	3.10
	Al 2024-T3	8.00	7.10	16.29	2.72	1.17	2.69
	Al 6061-T6	8.00	7.20	18.10	2.95	1.19	2.99
	Al 7075-T6	8.00	5.56	12.07	2.62	0.92	1.99
A3T26-3	Al 2024-O	8.00	4.58	16.21	1.81	0.56	2.00
	Al 2024-T3	8.00	4.42	13.15	1.62	0.55	1.62
	Al 6061-T6	8.00	4.21	15.13	1.72	0.52	1.87
	Al 7075-T6	8.00	2.91	9.30	1.57	0.36	1.15
A3T28-5	Al 2024-O	8.00	3.28	17.99	1.18	0.33	1.83
	Al 2024-T3	8.00	2.41	12.09	1.07	0.24	1.23
	Al 6061-T6	8.00	2.81	14.80	1.13	0.29	1.50
	Al 7075-T6	8.00	1.20	9.74	1.05	0.12	0.99
A4T32-4	Al 2024-O	8.00	9.48	24.29	3.35	1.62	4.15
	Al 2024-T3	8.00	8.52	16.42	2.72	1.46	2.81
	Al 6061-T6	8.00	8.04	19.12	3.04	1.37	3.27
	Al 7075-T6	8.00	4.91	12.57	2.60	0.84	2.15

A4T34-5	Al 2024-O	8.00	4.95	20.42	1.48	0.57	2.34
	Al 2024-T3	8.00	3.02	13.75	1.29	0.35	1.58
	Al 6061-T6	8.00	3.43	15.87	1.39	0.39	1.82
	Al 7075-T6	8.00	1.88	10.82	1.24	0.22	1.24
A4T36-2	Al 2024-O	8.00	2.36	18.41	0.82	0.21	1.60
	Al 2024-T3	8.00	1.21	13.49	0.74	0.11	1.18
	Al 6061-T6	8.00	1.45	15.64	0.78	0.13	1.36
	Al 7075-T6	8.00	0.47	10.44	0.72	0.04	0.91
A4T38-2	Al 2024-O	8.00	1.18	17.88	0.59	0.09	1.29
	Al 2024-T3	8.00	0.68	12.92	0.54	0.05	0.93
	Al 6061-T6	8.00	0.71	14.12	0.57	0.05	1.02
	Al 7075-T6	8.00	0.28	10.30	0.53	0.02	0.74
A5T42-4	Al 2024-O	8.00	7.62	23.63	3.40	1.02	3.17
	Al 2024-T3	8.00	5.26	16.30	2.77	0.71	2.19
	Al 6061-T6	8.00	5.51	18.67	3.09	0.74	2.50
	Al 7075-T6	8.00	2.92	12.53	2.64	0.39	1.68

Table 7: Effective strength values for FMLs of varying composition, based on rule of mixtures approximation.

Lay-ups	Total thickness (mm)	Thickness of aluminium (mm)	Thickness of GFPP (mm)	Aluminium type	Estimated static tensile strength (MPa)
GFPP	N/A	N/A	N/A	N/A	300
A2T18-4	5.60	1.27	4.33	Al 2024-O	274
				Al 2024-T3	342
				Al 6061-T6	302
				Al 7075-T6	362
A3T24-8	6.06	1.91	4.16	Al 2024-O	264
				Al 2024-T3	358
				Al 6061-T6	303
				Al 7075-T6	386
A3T26-3	8.10	1.91	6.20	Al 2024-O	273
				Al 2024-T3	343
				Al 6061-T6	302
				Al 7075-T6	364
A3T28-5	9.82	1.91	7.94	Al 2024-O	278
				Al 2024-T3	335
				Al 6061-T6	302
				Al 7075-T6	353
A4T32-4	5.85	2.54	3.31	Al 2024-O	251
				Al 2024-T3	379
				Al 6061-T6	304

				Al 7075-T6	418
A4T34-5	8.73	2.54	6.19	Al 2024-O	267
				Al 2024-T3	353
				Al 6061-T6	303
				Al 7075-T6	379
A4T36-2	11.48	2.54	8.94	Al 2024-O	275
				Al 2024-T3	340
				Al 6061-T6	302
				Al 7075-T6	360
A4T38-2	13.90	2.54	11.36	Al 2024-O	279
				Al 2024-T3	333
				Al 6061-T6	302
				Al 7075-T6	350
A5T42-4	7.46	3.18	4.29	Al 2024-O	251
				Al 2024-T3	378
				Al 6061-T6	304
				Al 7075-T6	416